Check for updates

Synergizing Phase and Cavity in $CoMoO_xS_y$ Yolk-Shell Anodes to Co-Enhance Capacity and Rate Capability in Sodium Storage

Jinkai Wang[1,2], Lei Zhu[1], Fang Li[1], Tianhao Yao[1], Ting Liu[1], Yonghong Cheng[1], Zongyou Yin[2]*, Hongkang Wang[1]*

[1]*State Key Lab of Electrical Insulation and Power Equipment, Center of Nanomaterials for Renewable Energy (CNRE), School of Electrical Engineering, Xi'an Jiaotong University, Xi'an, China 710049. E-mail: hongkang.wang@mail.xjtu.edu.cn*

[2]*Research School of Chemistry, Australian National University, Canberra, ACT 2601, Australia. E-mail: zongyou.yin@anu.edu.au*

Abstract. Sodium-ion batteries (SIBs) have been recognized as the promising alternatives to lithium-ion batteries (LIBs) for large-scale applications owing to their abundant sodium resource. Currently, one significant global challenge for SIBs thus was to explore feasible anode materials featured with high specific capacity and reversible pulverization-free Na^+ insertion and extraction. To overcome this problem, we herein developed a facile co-engineering on polymorph phases and cavity structures based on CoMo-glycerate by scalable solvothermal sulfidation. The optimized strategy enabled the construction of an amorphous yolk-shell $CoMoO_xS_y$ with synergized partially-sulfidized amorphous phase and yolk-shell confined cavity. After developed as the anodes for SIBs, such $CoMoO_xS_y$ electrode delivered a high reversible capacity of 479.4 mA h /g at 200 mA/g after 100 cycles and a high rate capacity of 435.2 mA h/g even at 2000 mA/g, demonstrating superior cycle stability and excellent rate capability. These are attributed to the unique dual merits of the anodes, i.e.

This is the author manuscript accepted for publication and has undergone full peer review but has not been through the copyediting, typesetting, pagination and proofreading process, which may lead to differences between this version and the Version of Record. Please cite this article as doi: 10.1002/smll.202002487.

This article is protected by copyright. All rights reserved.

Author Manuscript

the elastic bountiful reaction pathways favored by the sulfidation-induced amorphous phase and the sodiation/desodiation accommodatable space benefited from the yolk-shell cavity. Such yolk-shell nano battery materials are merited with co-tunable phases and structures, facile scalable fabrication, and excellent capacity and rate capability in sodium storage. This provides an opportunity to develop advanced practical electrochemical sodium storage in the future.

Keywords: Sodium-ion batteries; Co-engineering on polymorph phases and cavity structures; Amorphous yolk-shell $CoMoO_xS_y$; Electrochemical properties

Introduction.

Lithium-ion batteries (LIBs) have been widely used in portable electronic devices (*ex.*, mobile phones, and laptops) and large-scale energy storage systems (*ex.*, electric vehicles, and smart-grid) because of their high operating voltage, high energy density, low self-discharge and long lifespan.[1-4] However, the limited global lithium resources cannot achieve the sustainable development owing to the increasing large-scale demand in the energy storage market.[5-7] With the similar electrochemical reaction mechanism to that of LIBs, sodium-ion batteries (SIBs) have been regarded as a promising alternative owing to the abundant sodium resource, low-cost and proper redox potential, which are extremely suitable for large-scale application in smart-grid.[8, 9] The great obstacle for SIBs comes from the larger ionic radius of Na^+ (0.102 nm), which can be hardly inserted into the graphite anode with very few sodium storage capacity.[10, 11] Besides, exploring novel anode materials for SIBs also suffers from the intrinsic sluggish reaction kinetics and the large volume changes upon sodiation/desodiation, which are still challenging and needed to be overcome urgently.

As promising candidates for SIB anode materials, transition metal (ex., Co and Mo) sulfides have received considerable attention owing to their natural resource abundance, cheapness and high theoretical specific capacities.[12-15] However, the huge volume changes upon Na^+ insertion/extraction would produce great strain, which thus results in the pulverization problem of the electrode and eventually the rapid capacity fading.[16] To solve this problem, various strategies have been explored, including morphological, compositional and phase engineering of the electrode materials especially in nanoscale. On one hand, nanostructuring has been considered as an effective strategy, which can shorten the sodium ion diffusion paths, enlarge the contact between the electrode

This article is protected by copyright. All rights reserved.

Author Manuscript

and electrolyte, and facilitate the fast electron/ion transport.[17-19] To date, various nanostructured metal sulfides (*ex.*, nanospheres, nanosheets, and nanoflowers) have been prepared and applied as SIB anodes.[20-22] Especially, yolk-shell structured materials have attracted numerous attention for sodium storage, in virtue of the unique cavity structure between the yolk and shell, which can buffer the volume changes upon sodiation/desodiation and thus alleviate the electrode pulverization problem.[23, 24] For example, Choi *et al.* have successfully constructed SnS-MoS_2 yolk-shell microspheres which demonstrated superior sodium storage properties and high structural stabilities upon cycling, as compared to the solid microspheres.[25] Chen *et al.* reported the fabrication of the yolk-shell NiS_2 nanoparticles in the porous carbon fibers and constructed a flexible fiber-shaped sodium battery, which displayed outstanding sodium storage properties with high specific capacity, ultrastable cycling stability and high rate capability.[26] Wang *et al.* also prepared a yolk-shell Co_9S_8/MoS_2 polyhedron hybridized with N-doped carbon matrices deriving from a metal-organic framework precursor, which exhibited impressive rate capability and cycling performance.[27]

On the other hand, engineering the phase, composition and crystallinity of the electrode materials is another effective strategy to enhance their electrochemical properties. Compared to metal oxides, metal sulfides generally exhibit better sodium storage performances due to their suitable redox potentials and higher intrinsic conductivity.[28, 29] Additionally, multiple composition hybridization can bring more structural defects and decrease the ion insertion barriers, which facilitate to enhance the electrochemical performance because of the largely increased electrochemically active sites, and the potential synergistic enhancement effect arising from step-wise reaction mechanism.[30, 31] Instead of preparing crystalline materials, developing amorphous anode materials with disordered structure has attracted considerable attentions owing the unique merits, such as the increased active sites, multiple ion diffusion pathways, reversed lattice variations and volumetric changes during the ion insertion/extraction processes.[32, 33]

Herein, with combination of all the above enhancing strategies, we demonstrated the successful construction of amorphous yolk-shell bimetallic Co/Mo hybrid oxides/sulfides (denote as Y-$CoMoO_xS_y$) nanospheres, derived from the solid CoMo-glycerate nanospheres which were prepared *via* glycerol-assisted solvothermal method. Owing to the unique structure of glycerol, the large hydrogen bonds can easily combine with metal ions, forming metal-glycerol chelating compounds, which have been widely used to fabricate novel nanostructured inorganic materials.[34-36] In this work, we systematically investigated the use of CoMo-glycerate to synthesize the yolk-shell $CoMoO_4$ nanospheres (denote as Y-$CoMoO_4$) *via* directly annealing in air,

Author Manuscript

This article is protected by copyright. All rights reserved.

and the yolk-shell or hollow $CoMoO_xS_y$ hybrid nanospheres *via* sulfurization under solvothermal condition using thioacetamide (TAA) as sulfur source. When studied as anodes for SIBs, the as-obtained amorphous yolk-shell $CoMoO_xS_y$ nanospheres demonstrated better cycle stability and rate performance.

Results and Discussion.

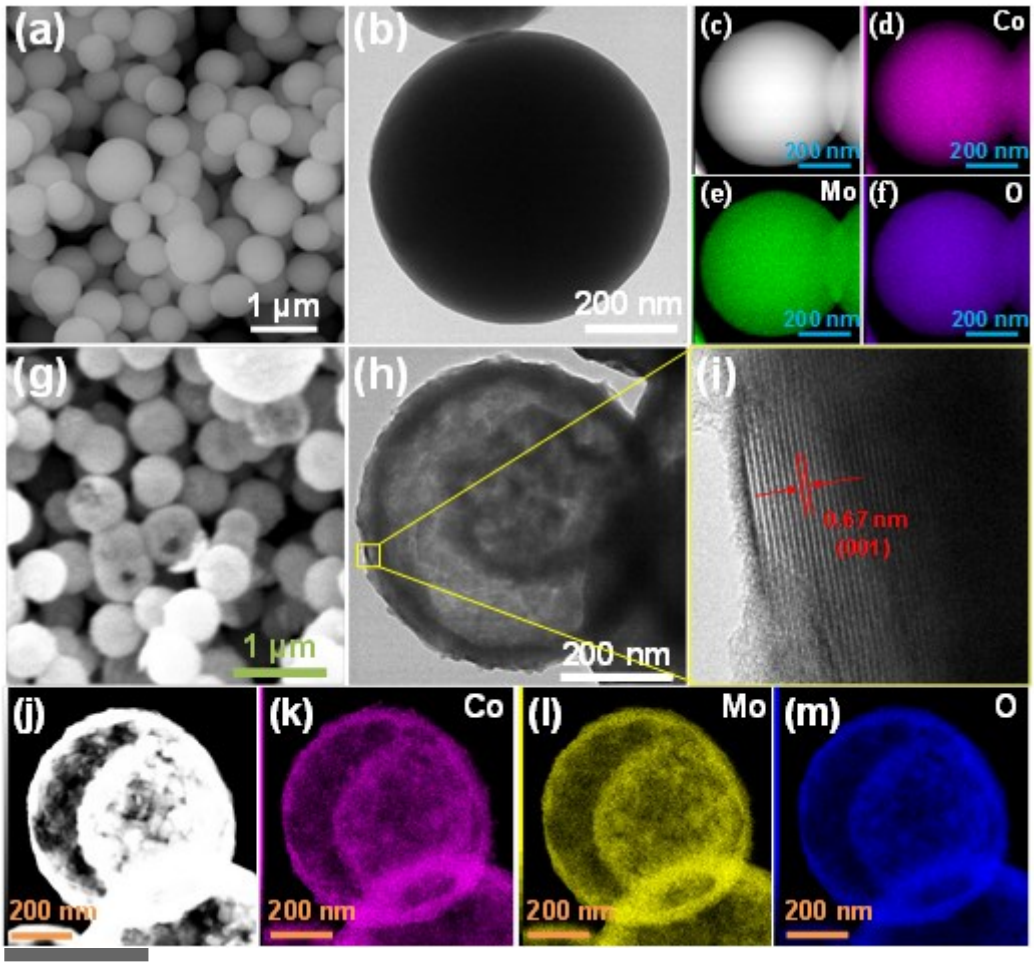

Figure 1. (a) SEM and (b) TEM images of solid CoMo-glycerate nanospheres, and (c) HAADF-STEM image of a single CoMo-glycerate nanosphere with corresponding EDS maps of (d) Co, (e) Mo and (f) O elements. (g) SEM and (h) TEM images of Y-$CoMoO_4$ nanospheres, and (i) HRTEM image of Y-$CoMoO_4$ nanospheres taken from the selected area of (h). (j) HAADF-STEM

This article is protected by copyright. All rights reserved.

image of a single Y-$CoMoO_4$ nanosphere with corresponding EDS maps of (k) Co, (l) Mo and (m) O elements.

Manuscript

Figures 1a and b showed the SEM and TEM images of CoMo-glycerate precursor, which displayed solid nanosphere morphology with uniform diameters of 500-700 nm and smooth surfaces. High-angle annular dark-field scanning transmission electron microscopy (HAADF-STEM) image and corresponding EDS mapping revealed the uniform distribution of Co, Mo and O elements within a single nanosphere (Figure 1c-f). After annealing in the air, CoMo-glycerate decomposed and converted into Y-$CoMoO_4$ with conformal nanosphere morphology, but the solid structure converted into yolk-shell structure (Figure 1g-h), following the inside-out Oswald ripening mechanism.[37] HRTEM image of Y-$CoMoO_4$ displayed distinct lattice fringes with *d* spacing of 0.67 nm (Figure 1i), which can be indexed to the (001) plane of the monoclinic $CoMoO_4$ phase,[38, 39] consistent with the XRD analysis (will be discussed later). To further confirm the element distribution and the yolk-shell structure of Y-$CoMoO_4$ nanospheres, HAADF-STEM image and corresponding EDS maps were taken on a single Y-$CoMoO_4$ nanosphere (Figure 1j-m), which obviously revealed that Co, Mo and O elements were homogeneously distributed on the yolk and shell of the nanosphere with good overlapping.

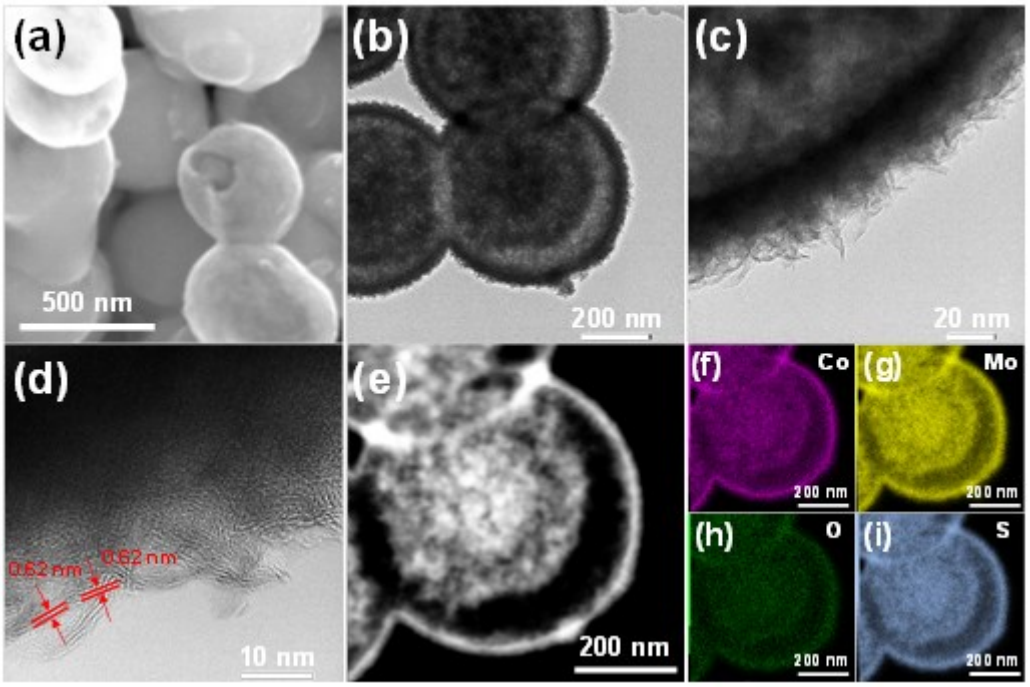

This article is protected by copyright. All rights reserved.

Figure 2. (a) SEM, (b, c) TEM and (d) HRTEM images of Y-$CoMoO_xS_y$ nanospheres. (e) HAADF-STEM image of a single Y-$CoMoO_xS_y$ nanosphere with corresponding EDS maps of (f) Co, (g) Mo, (h) O and (i) S elements.

Sulfurization of CoMo-glycerate under solvothermal condition using TAA as sulfur source resulted in the formation of yolk-shell Y-$CoMoO_xS_y$ which can be regarded as hybrid Co/Mo oxides/sulfides. SEM image revealed that Y-$CoMoO_xS_y$ displayed the conformal nanosphere morphology (Figure 2a), similar with that of CoMo-glycerate, but the surface became rough. Some broken spheres in Figure 2a and the TEM image (Figure 2b) demonstrated that the Y-$CoMoO_xS_y$ nanospheres displayed a unique yolk-shell structure, and the thickness of the outer shell of Y-$CoMoO_xS_y$ was around 30 nm (Figure 2c). In addition, series of slim nanoclusters were grown on the shell surface with lengths of about 10 nm and thickness of several nanometers (Figure 2c). HRTEM image clearly showed the well-defined lattice fringes with *d* spacing of 0.62 nm (Figure 2d), which can be ascribed to the (002) plane of MoS_2.[40-42] The HAADF-STEM image with corresponding EDS maps taken on a single Y-$CoMoO_xS_y$ nanosphere revealed that Co, Mo, O and S elements were well overlapped and uniformly distributed within the yolk-shell nanosphere (Figure 2e-i), suggesting the formation of Co/Mo oxides/sulfides.

Hollow H-$CoMoO_xS_y$ nanospheres were also prepared by prolonging the sulfurization duration to 6h, and Figure 3a showed the well-defined spherical morphology with rough surface. Differently, H-$CoMoO_xS_y$ exhibited a hollow structure with yolk completely disappeared, and the average thickness of the shell was around 30 nm (Figure 3b, c). As compared with Y-$CoMoO_xS_y$, the sheet-like crystallites on the surface of the nanosphere became shorter and wider, but the lattice fringes with *d* spacing of 0.62 nm belonging to MoS_2 can still be well observed in the HRTEM image (Figure 3d). HAADF-STEM image and corresponding EDS maps of a single H-$CoMoO_xS_y$ nanosphere demonstrated the disappearance of the yolk structure (Figure 3e-i), as Co, Mo, O and S elements were mainly distributed within the shells.

Author Manuscript

This article is protected by copyright. All rights reserved.

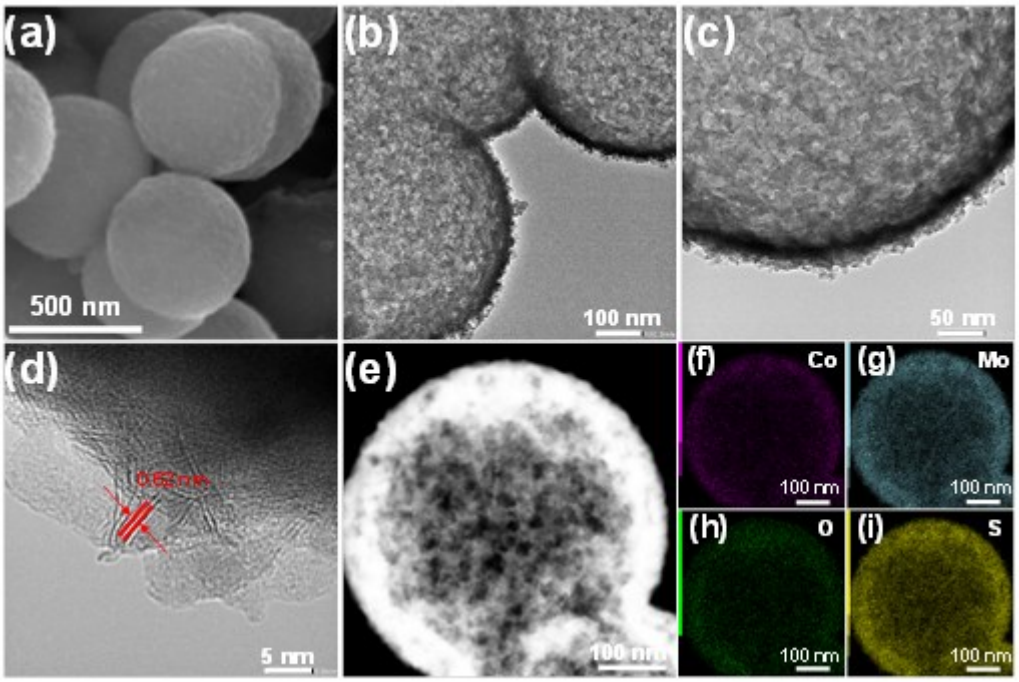

Figure 3. (a) SEM, (b, c) TEM and (d) HRTEM images of the H-$CoMoO_xS_y$ nanospheres. (e) HAADF-STEM image of a single H-$CoMoO_xS_y$ nanosphere with corresponding EDS maps of (f) Co, (g) Mo, (h) O and (i) S elements.

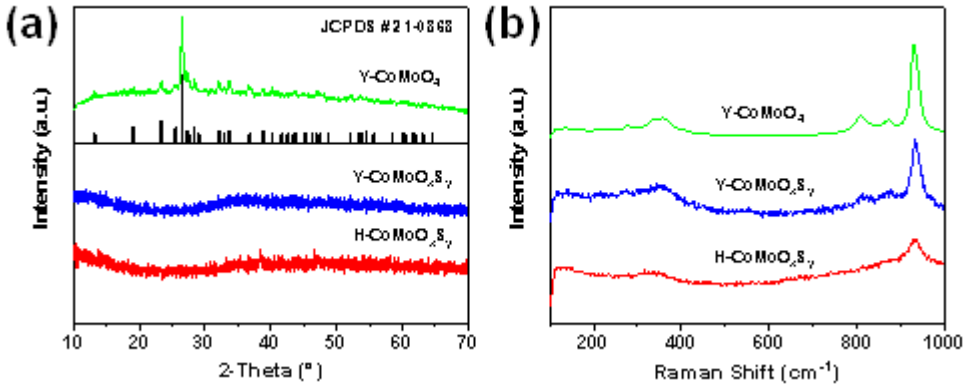

Figure 4. (a) XRD patterns and (b) Raman spectra of Y-$CoMoO_4$, Y-$CoMoO_xS_y$ and H-$CoMoO_xS_y$ nanospheres.

This article is protected by copyright. All rights reserved.

Figure 4a showed the XRD patterns of the Y-$CoMoO_4$, Y-$CoMoO_xS_y$ and H-$CoMoO_xS_y$ nanospheres. Y-$CoMoO_4$ exhibited well-defined diffraction peaks which can be indexed to the monoclinic $CoMoO_4$ phase (JCPDS No. 21-0868). In contrast, no obvious diffraction peaks can be observed in the XRD patterns of Y-$CoMoO_xS_y$ and H-$CoMoO_xS_y$, even though those MoS_2 crystallites were observed in the HRTEM image, which may be attributed to the interruption of the Co/Mo oxides/sulfides and the amorphous nature of some components.[43-45] Figure 4b compared the Raman spectra of Y-$CoMoO_4$, Y-$CoMoO_xS_y$ and H-$CoMoO_xS_y$ nanospheres. For Y-$CoMoO_4$, the apparent peaks at 336, 361, 812, 874 and 932 cm^{-1} can be ascribed to the Mo-O-Co stretching vibrations in $CoMoO_4$.[39, 46] For Y-$CoMoO_xS_y$ and H-$CoMoO_xS_y$, the intensities of the peaks belonging to Co-Mo-O became weaker and weaker with increasing sulfurization durations, which may suggest a gradual conversion from Co/Mo oxides to sulfides, and this was consistent with the fact that the oxygen content in H-$CoMoO_xS_y$ is less than that in Y-$CoMoO_xS_y$.

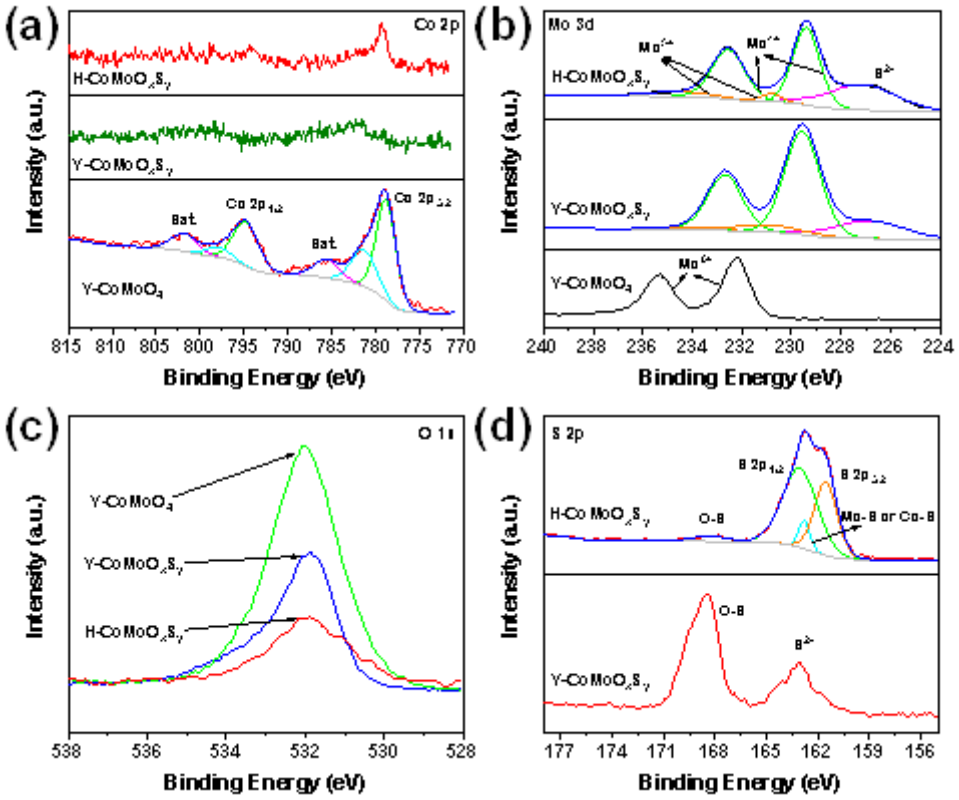

Figure 5. (a) Co 2p, (b) Mo 3d and (c) O 1s XPS spectra of Y-$CoMoO_4$, Y-$CoMoO_xS_y$ and H-$CoMoO_xS_y$ nanospheres. (d) S 2p XPS spectra of Y-$CoMoO_xS_y$ and H-$CoMoO_xS_y$ nanospheres.

This article is protected by copyright. All rights reserved.

X-ray photoelectron spectroscopy (XPS) was performed to study the chemical compositions and chemical states of Y-$CoMoO_4$, Y-$CoMoO_xS_y$ and H-$CoMoO_xS_y$ nanospheres (Figure 5). As shown in Figure 5a, the Co 2p spectrum of Y-$CoMoO_4$ showed four peaks at 779.0, 785.7, 795.1 and 801.8 eV, which can be correspondingly assigned to the Co $2p_{3/2}$, the shake-up satellite peak, Co $2p_{1/2}$ and the shake-up satellite peak.[47-49] In contrast, the peaks in Y-$CoMoO_xS_y$ and H-$CoMoO_xS_y$ were very weak and only two peaks appear at 779.4 and 794.2 eV, which can be ascribed to the superficial cobalt oxide.[50] This could be due to that cobalt sulfides were susceptible to be oxidized in air according to the previous literatures.[51, 52] In the Mo 3d XPS spectrum of Y-$CoMoO_4$ (Figure 5b), two prominent peaks at the binding energies of 232.2 and 235.3 eV were assigned to the Mo $3d_{5/2}$ and Mo $3d_{3/2}$, indicating the oxidation state of Mo^{6+},[48] while the two prominent peaks in Y-$CoMoO_xS_y$ and H-$CoMoO_xS_y$ located at around 228.7 eV and 231.9 eV, suggesting the presence of Mo^{4+} and the formation of MoS_2. Besides, the peak at around 225.7 eV corresponded to S^{2-},[53] which became stronger in the H-$CoMoO_xS_y$, properly suggesting the increase of sulfide content. Besides, the molybdenum with Mo^{4+} and Mo^{5+} valence states can be roughly estimated as 88.5% and 11.5% (by areas beneath XPS peaks) from the Mo 3d XPS patterns after deconvolution, which was assigned to MoS_2 and Mo_2O_5, respectively. As compared with that of Y-$CoMoO_4$, the intensities of O1s peak for Y-$CoMoO_xS_y$ and H-$CoMoO_xS_y$ greatly decreased with increasing sulfurization duration (Figure 5c), suggesting the decrease of oxygen content in the hybrid. In the S 2p spectrum for Y-$CoMoO_xS_y$, the peaks at the binding energies of 163.2 and 168.5 eV corresponded to the O-S bond and S^{2-}, respectively.[54] In H-$CoMoO_xS_y$, the peak of O-S became weakened and almost disappeared, while the S^{2-} peak can be deconvoluted into two peaks at 161.7 and 162.8 eV, which can be assigned to S $2p_{3/2}$ and S $2p_{1/2}$, respectively.[55] As a result, XPS analysis further confirmed the gradual conversion from oxides to sulfides and the eventual formation of $CoMoO_xS_y$ hybrid. This was confirmed by the measured O/S atomic ratio according to the XPS analysis, as shown in Table S2, where we can see that the O/S atomic ratios decreased greatly from 3.94 to 0.615 with extending the sulfurization duration, suggesting the increase of the S content and the decrease of the O content.

Author Manuscript

This article is protected by copyright. All rights reserved.

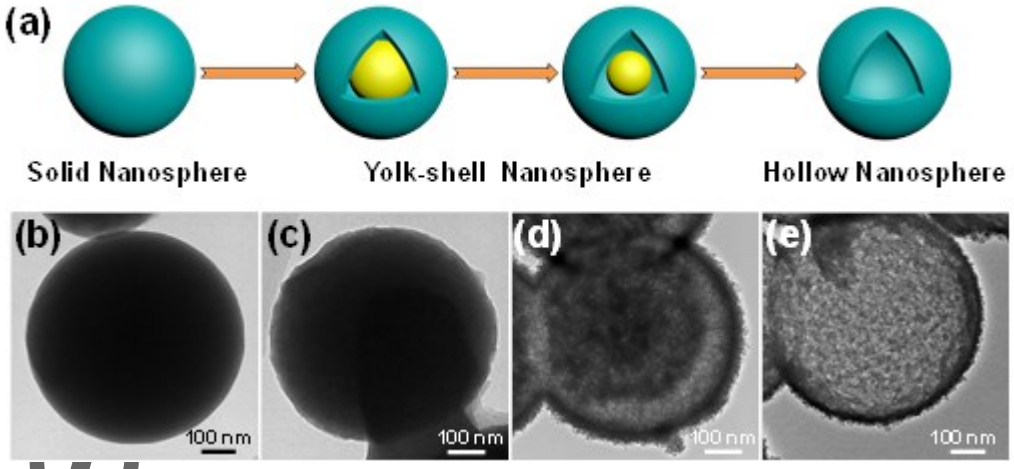

Figure 6. (a) Schematic illustration of the evolutions from solid CoMo-glycerate nanospheres to yolk-shell and hollow $CoMoO_xS_y$ nanospheres. (b-d) TEM images for (b) CoMo-glycerate solid nanospheres and the resulting products after TAA sulfurization for different solvothermal reaction times: (c) 0.5 h, (d) 2 h, (e) 6 h.

The formation mechanism of the yolk-shell and hollow $CoMoO_xS_y$ nanospheres was investigated *via* a time-dependent experiment, in which the sulfidation process of CoMo-glycerate precursor was controlled by adjusting the solvothermal reaction time. As schematically illustrated in Figure 6a, the solid CoMo-glycerate nanospheres gradually converted into yolk-shell and finally hollow $CoMoO_xS_y$ nanospheres, with the presence of TAA as a sulfurization agent. Under the solvothermal condition, TAA would firstly decompose and release the S^{2-} ions at high temperature, and then S^{2-} preferentially reacted with the solid CoMo-glycerate nanospheres at the surface region, forming rigid metal sulfides. During this inside-out Oswald ripening process, they would gradually form a gap between the inward yolk and the outward shell.[56] TEM images clearly reflected the structural evolutions from solid CoMo-glycerate nanospheres to yolk-shell and hollow $CoMoO_xS_y$ nanospheres (Figure 6b-e). When the solvothermal reaction time was short (0.5 h), the yolk-shell structure started to form and the small gap cannot be obviously observed from the TEM image (Figure 6c). However, the HAADF-STEM image and corresponding EDS maps apparently confirmed the yolk-shell structure, and the Co, Mo, O and S elements were uniformly distributed within the yolk-shell nanosphere (Figure S1). With prolonging the sulfurization time, the gap between the yolk and shell gradually increased with the

Author Manuscript

This article is protected by copyright. All rights reserved.

consumption of the inner yolk, finally forming the yolk-shell nanosphere (Figure 6d) and the hollow nanosphere (Figure 6e).

In order to study the correlation between sulfurization temperature and morphology microstructure of the $CoMoO_xS_y$ nanospheres, the experiments at different temperatures (120 °C, 140 °C, 180 °C and 200 °C) were performed. As shown in the TEM images in Figure S8, it is clear that all the $CoMoO_xS_y$ nanospheres displayed unique yolk-shell structures, suggesting that the reaction temperature has little effect on the particle size and structure of the $CoMoO_xS_y$.

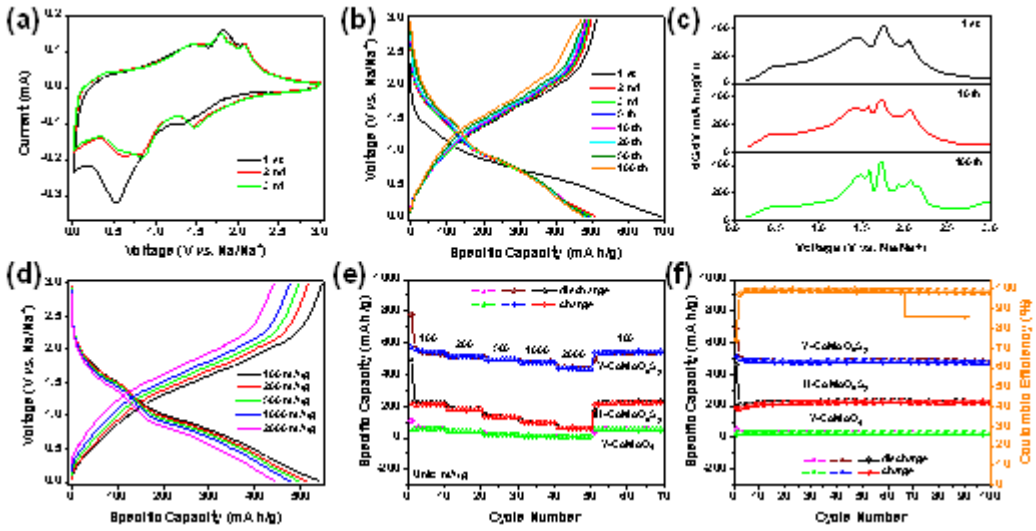

Figure 7. Electrochemical properties of the Y-$CoMoO_4$, Y-$CoMoO_xS_y$ and H-$CoMoO_xS_y$ electrodes. (a) CV curves of the Y-$CoMoO_xS_y$ electrode for the first 3 cycles at a scan rate of 0.2 mV/s in the range of 0.01-3.0 V. (b) Galvanostatic discharge/charge profiles of the Y-$CoMoO_xS_y$ electrode at 200 mA/g. (c) Differential charge capacity *versus* voltage plots at different cycles. (d) Discharge-charge profiles of the Y-$CoMoO_xS_y$ electrode at different current densities. (e) Rate performances of the Y-$CoMoO_4$, Y-$CoMoO_xS_y$ and H-$CoMoO_xS_y$ electrodes at different current densities. (f) Cycle performances for the Y-$CoMoO_4$, Y-$CoMoO_xS_y$ and H-$CoMoO_xS_y$ electrodes with the corresponding Coulombic efficiencies (CE) for the Y-$CoMoO_xS_y$ electrode at 200 mA/g.

To demonstrate their efficacy as anodes for sodium storage, the electrochemical properties of the Y-$CoMoO_4$, Y-$CoMoO_xS_y$ and H-$CoMoO_xS_y$ electrodes were investigated in coin-type half-cells using sodium foil as the counter and reference electrode. Figure 7a displayed the cyclic

This article is protected by copyright. All rights reserved.

voltammogram (CV) curves of the Y-$CoMoO_xS_y$ electrode for the first 3 cycles at a scan rate of 0.2 mV/s. The peak at around 1.31 V in the first cathodic scan can be attributed to the sodiation of MoS_2 to Na_xMoS_2 ($MoS_2 + xNa^+ + xe^- \rightarrow Na_xMoS_2$) and CoS_2 to Na_xCoS_2 ($CoS_2 + xNa^+ + xe^- \rightarrow Na_xCoS_2$). Besides, the broad and prominent peak centered at around 0.52 V corresponded to the conversion reactions from Na_xMoS_2 to metallic Mo ($Na_xMoS_2 + (4-x)Na^+ + (4-x)e^- \rightarrow Mo + 2Na_2S$) and Na_xCoS_2 to metallic Co ($Na_xCoS_2 + (4-x)Na^+ + (4-x)e^- \rightarrow Co + 2Na_2S$), accompanying with the decomposition of the electrolyte to irreversibly form the solid electrolyte interface (SEI) film.[16, 45] In the first anodic scan, there were four peaks located at about 0.41, 1.49, 1.82 and 2.08 V, which can be ascribed to the oxidation reaction of metallic molybdenum to Na_xMoS_2 ($Mo + 2Na_2S \rightarrow Na_xMoS_2 + (4-x)Na^+ + (4-x)e^-$), the desodiation process from Na_xMoS_2 to MoS_2 ($Na_xMoS_2 \rightarrow MoS_2 + xNa^+ + xe^-$), and the similar stepwise oxidation reaction and desodiation process associated with the metallic cobalt to CoS_2 ($Co + 2Na_2S \rightarrow Na_xCoS_2 + (4-x)Na^+ + (4-x)e^-$, $Na_xCoS_2 \rightarrow CoS_2 + xNa^+ + xe^-$), respectively. In the subsequent cycles, the two cathodic peaks shifted to higher voltages, which may be attributed to the activation process and the structural variation of the Y-$CoMoO_xS_y$ electrode after the first CV cycle.[57] Since the second CV cycle onward, the profiles were well overlapped, suggesting the good reversibility of the electrochemical reactions in the Y-$CoMoO_xS_y$ electrode.

Figure 7b showed the discharge/charge profiles of the Y-$CoMoO_xS_y$ electrode at 200 mA/g, which delivered the initial discharge/charge capacities of 692.2/520.0 mA h/g with a high initial Coulombic efficiency (ICE) of 73.96 %. The large capacity loss in the first cycle was a common phenomenon in various SIB anodes such as $MoSe_2$, SnO_2 and MoO_2 due to the formation of SEI film and the decomposition of electrolyte in the low voltage range.[58-60] Besides, the exposed large surface area (~24.7 m^2/g, shown in Figure S5) of the Y-$CoMoO_xS_y$ electrode maybe also influence the ICE.[61] In the following cycles, the CEs of the Y-$CoMoO_xS_y$ electrode can maintain at about 99% after 100 cycles, indicating the good reversibility. Figure 7c showed the differential charge capacity versus voltage plots, and four peaks in the first charge process were well consistent with the CV analysis. A new peak at 1.61 V emerged in the 10^{th} cycle, and all the five peaks remained in the 100^{th} cycle, suggesting the highly reversibility of the oxidation/desodiation reactions.[62] Besides, two peaks appeared at around 1.94 and 2.16 V became obviously visible in the 100^{th} cycles, which can be ascribed to the oxidization process of metallic Co species.[63, 64]

Figure 7d presented the discharge-charge profiles of the Y-$CoMoO_xS_y$ electrode at different current densities ranging from 100 to 2000 mA/g. It was observed that the small increase in the charge plateau illustrated the rapid reaction kinetics and the low polarization of the Y-$CoMoO_xS_y$

Author Manuscript

This article is protected by copyright. All rights reserved.

electrode.[65] Figure 7e compared the rate performances of the Y-$CoMoO_4$, Y-$CoMoO_xS_y$ and H-$CoMoO_xS_y$ electrodes with current densities ranging from 100 to 2000 mA/g. The Y-$CoMoO_4$ electrode displayed extremely small sodium storage capacities of 61.4, 39.8, 20.0, 11.3 and 6.1 mA h/g at current densities of 100, 200, 500, 1000 and 2000 mA/g each after 10 cycles, respectively, while the H-$CoMoO_xS_y$ electrode exhibited slightly increased discharge capacities of 219.5, 181.0, 130.9, 94.9 and 59.5 mA h/g at the same condition. Interestingly, the Y-$CoMoO_xS_y$ electrode displayed much higher reversible capacities of 531.2, 511.7, 497.3, 480.7 and 435.2 mA h/g at progressively increased current densities from 100 to 200, 500, 1000 and 2000 mA/g, respectively. Even recovering the current density from 2000 to 100 mA/g, the Y-$CoMoO_xS_y$ electrode still maintained a discharge capacity of 540.6 mA h/g after another 20 cycles, which was much higher than that of the Y-$CoMoO_4$ and H-$CoMoO_xS_y$ electrodes, suggesting the best rate capability of the H-$CoMoO_xS_y$ electrode.

Figure 7f compared the cycle performances of the Y-$CoMoO_4$, Y-$CoMoO_xS_y$ and H-$CoMoO_xS_y$ electrodes at 200 mA/g. The Y-$CoMoO_xS_y$ electrode delivered a high discharge capacity of 479.4 mA h/g at 200 mA/g after 100 cycles, much higher than that of the Y-$CoMoO_4$ (26.9 mA h/g) and H-$CoMoO_xS_y$ electrodes (227.7 mA h/g). Furthermore, when at a higher current density (1000 mA/g), the Y-$CoMoO_xS_y$ electrode delivered a high discharge capacity of ~403 mA h/g at 1000 mA/g after 100 cycles (Figure S6). The superior sodium storage performance of the Y-$CoMoO_xS_y$ electrode, including higher specific capacity, better cycling stability and rate capability, could be ascribed to the synergistic enhancement effect of the unique yolk-shell nanosphere architecture and the amorphous Co/Mo oxides/sulfides. The inner yolk of the yolk-shell nanospheres can largely increase electrochemically active sites for intercalating sodium ions and thus enlarge the energy density of the whole electrode;[66, 67] In addition, the middle cavity between yolk and shell can prevent the volume change of electrodes during the charge and discharge processes, and thus suppress the pulverization of electrodes.[68, 69] Additionally, the amorphous structure with disordered lattices can provide multiple Na^+ diffusion pathways and more electrochemically active sites for Na^+ intercalation,[66, 67] and showed reversed lattice variations and volumetric changes upon sodiation/desodiation, thus facilitating to alleviate the volume changes. Moreover, electrochemical impedance spectroscopy (EIS) was carried out to investigate the charge transfer kinetics of the Y-$CoMoO_xS_y$ electrode (Figure S2). The charge transfer resistance (R_{ct}) at the high frequency region for the Y-$CoMoO_xS_y$ electrode was around 286 Ω before cycling, and then reduced to 97 Ω after cycling, which indicated the fast charge transfer. Besides, the steeper inclined line at the low frequency region suggested the fast ion diffusion

Author Manuscript

This article is protected by copyright. All rights reserved.

rate in the Y-$CoMoO_xS_y$ electrode. As compared with the previously reported cobalt-based and molybdenum-based anodes for SIBs (Table S1), the Y-$CoMoO_xS_y$ electrode demonstrated outstanding sodium storage performance, indicating the high potential of the yolk-shell nanostructures as high-performance anodes for SIBs.

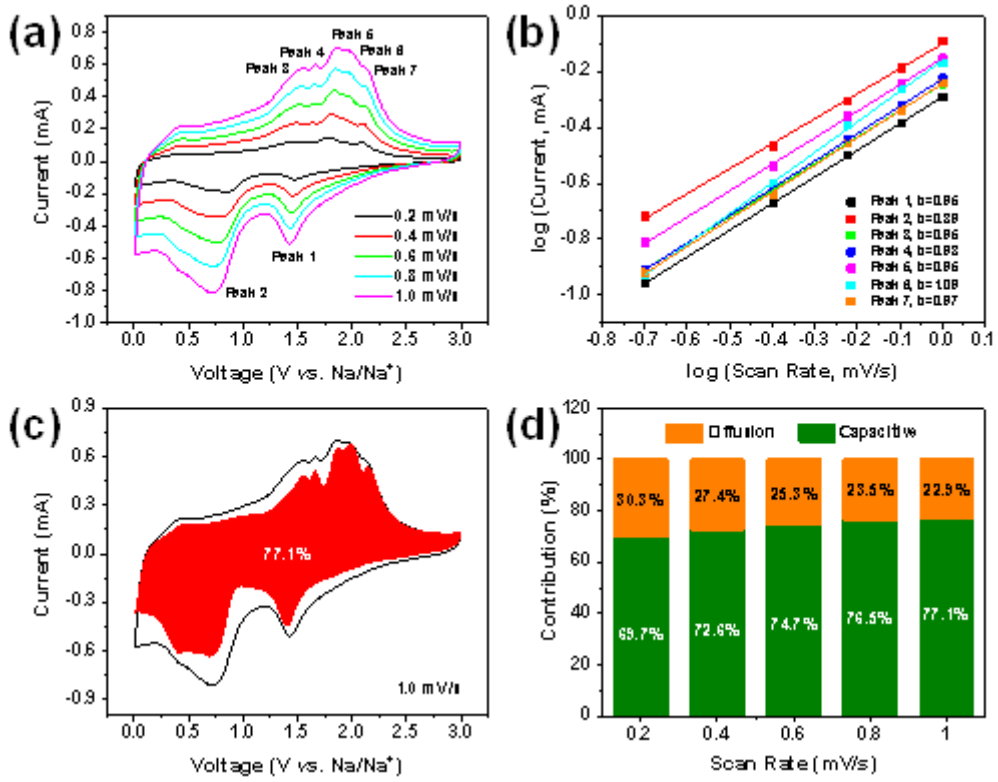

Figure 8. Quantitative capacitive analysis of sodium storage behavior for the Y-$CoMoO_xS_y$ electrode. (a) CV curves at various scan rates from 0.2 mV/s to 1.0 mV/s. (b) The corresponding logarithm peak current *versus* logarithm scan rate plots. (c) Separation of capacitive contribution (red region) and diffusion contribution at 1.0 mV/s. (d) Pseudocapacitive contribution ratio at different scan rates.

Figure 8a showed the CV curves at different scan rates ranging from 0.2 to 1.0 mV/s, in order to investigate the reaction kinetics of the Y-$CoMoO_xS_y$ electrode. Two cathodic peaks (Peak 1, Peak 2) and five anodic peaks (Peak 3-Peak 7) in each CV curve can be obviously observed, and the peak current increased with increasing the scan rates, which implied a pseudocapacitive behavior.[70] The

This article is protected by copyright. All rights reserved.

relationship between the peak current (i) and the scan rate (v) can be described by the following formula: $i = av^b$ (namely, $\log(i) = \log(a) + b \log(v)$), where b is an indicator of the charge storage mechanism, either pseudocapacitive or diffusion-controlled. When b value equals 0.5, it indicates that the electrochemical reaction is mainly diffusion-controlled, while b close to 1 indicates the electrochemical reaction is mainly a pseudocapacitive process.[71-73] The b value can be obtained from the logarithm peak current *versus* logarithm scan rate plots of the Y-$CoMoO_xS_y$ electrode, as shown in Figure 8b. The b values are the slopes of the linear fitted lines for the seven peaks (Peak 1-Peak 7), which are as 0.95, 0.89, 0.95, 0.98, 0.95, 1.09 and 0.97, respectively. This result suggested that the electrochemical behavior of the Y-$CoMoO_xS_y$ electrode was mainly controlled by the capacitive processes, which contributed to the superior rate/cycle performance. In order to further quantitatively determine the capacitive contribution in the Y-$CoMoO_xS_y$ electrode, the current can be separated into the capacitance-controlled (k_1v) and diffusion-controlled ($k_2v^{1/2}$), which can be expressed by the following formula: $i = k_1v + k_2v^{1/2}$ (k_1 and k_2 are constants).[74, 75] Figure 8c displayed the separated capacitive current (red region) contribution in the total current at different potential, and the capacitive contribution was as high as 77.1 % at the scan rate of 1.0 mV/s. Figure 8d compared the capacitive contribution at each scan rate, which increased from 69.7% to 77.1% with increasing the scan rate from 0.2 to 1.0 mV/s, further suggesting the high contribution of the pseudocapacitive mechanism.

In order to reveal the structural stability of the Y-$CoMoO_xS_y$ electrode upon cycling, SEM analysis was performed on the cycled electrode (as shown in Figure S9). It's clearly observed that the Y-$CoMoO_xS_y$ electrode still shows the well-defined sphere-like morphology even after 100 cycles at 200 mA/g, suggesting the structural stability of the yolk-shell $CoMoO_xS_y$ nanosphere. Importantly, the SEM taken from a broken sphere still exhibits the yolk-shell morphology, which further implies its capability in self-maintaining the yolk-shell structure during battery operation.

Conclusions.

In summary, we demonstrated the fabrication of amorphous yolk-shell Co-Mo oxide/sulfide nanospheres (Y-$CoMoO_xS_y$) *via* solvothermal sulfurization of CoMo-glycerate using TAA as sulfur source. The gap between yolk and shell can be feasibly controlled by adjusting the solvothermal reaction time. As SIB anode materials, the Y-$CoMoO_xS_y$ electrode demonstrated superior sodium storage performance, delivering a higher discharge capacity of 479.4 mA h /g at 200 mA/g after 100

Author Manuscript

This article is protected by copyright. All rights reserved.

cycles and a higher rate capacity of 435.2 mA h/g at 2000 mA/g, which were much higher than that of the $CoMoO_4$ (26.9 mA h/g after 100 cycles) and the hollow $CoMoO_xS_y$ electrodes (227.7 mA h/g after 100 cycles). The much enhanced sodium storage performance of the Y-$CoMoO_xS_y$ electrode could be ascribed to its unique yolk-shell nanosphere architecture and the amorphous structure. Specifically, the amorphous structure can provide multiple pathways for ions and facilitate the Na^+ diffusion, while the unique yolk-shell nanostructure can not only bring more electrochemically active sites, but also sufficiently shorten the sodium ion diffusion paths. In addition, the gap between yolk and shell can efficiently buffer the volumetric changes upon sodiation/desodiation. More importantly, this work opened an avenue to explore other high-performance amorphous anodes for SIBs with unique yolk-shell nanostructures, which promise the development of advanced electrochemical energy storage in the future.

Experimental Section.

Materials synthesis. All the chemicals were used as received without any further purification. Firstly, CoMo-glycerate nanospheres were synthesized as the precursors for the yolk-shell $CoMoO_xS_y$ hybrid nanostructures. In a typical synthesis, 0.2 mmol cobaltous nitrate hexahydrate ($Co(NO_3)_2 \cdot 6H_2O$, Macklin, 99%), 0.2 mmol molybdenum acetylacetone ($C_{10}H_{16}MoO_6$, Macklin, 97%) and 4 mL glycerol ($C_3H_8O_3$, Macklin, 99%) were dissolved in 30 mL isopropanol ($(CH_3)_2CHOH$, Macklin, 99.5%) under vigorous stirring, forming a pink transparent solution, which was then transferred into a 50 mL Teflon tank sealed with stainless steel autoclave and heated at 180 °C for 24 h. After naturally cooling to room temperature, the brown precipitate was washed with ethanol for three times *via* centrifugation, and thus the collected CoMo-glycerate product was dried at 60 ^oC overnight.

Syntheiss of yolk-shell $CoMoO_4$ nanospheres (denote as Y-$CoMoO_4$). Y-$CoMoO_4$ was directly synthesized by annealing the as-prepared CoMo-glycerate nanospheres at 550 °C for 2 h in a muffle furnace with a heating rate of 1 °C/min.

Synthesis of yolk-shell $CoMoO_xS_y$ hybrid nanospheres (denote as Y-$CoMoO_xS_y$). Sulfurization of CoMo-glycerate was performed *via* solvothermal method to obtain the Y-$CoMoO_xS_y$ hybrid. In a typical synthesis, 30 mg CoMo-glycerate nanospheres were ultrasonically dispersed in 30 mL ethanol for 30 min, and then 50 mg thioacetamide (TAA, Macklin, 99%) was added into the above suspension. Afterwards, the mixed solution was transferred to a 50 mL Teflon tank sealed with

Author Manuscript

This article is protected by copyright. All rights reserved.

stainless steel autoclave and heated at 160 °C for 2h. After cooling down naturally, the precipitate was collected and washed with ethanol for three times *via* repeated centrifugation, and then dried in an oven at 60 °C overnight. Finally, the Y-$CoMoO_xS_y$ hybrid nanospheres were obtained by further annealing the above precipitate at 300 °C for 2 h under Ar atmosphere with a heating rate of 1 °C/min. For comparison, hollow $CoMoO_xS_y$ hybrid nanospheres (denote as H-$CoMoO_xS_y$) were also prepared by increasing the solvothermal reaction time from 2h to 6h, while keeping other parameters constant during the synthesis.

Materials Characterization. The morphological structures and the fine microstructures of the products were characterized by scanning electron microscope (SEM, FEI Quanta 250F) and transmission electron microscope (TEM, JEOL JEM 2100) as well as high-resolution TEM (HRTEM). The high-angle annular dark field scanning transmission electron microscopy (HAADF-STEM) was conducted (JEOL JEM-F200 (HR)), and the energy-dispersive X-ray spectroscopy (EDS) was also performed for elemental analysis. X-ray diffraction (XRD) patterns of the products were characterized on a Bruker D2 PHASER X-ray diffractometer with Cu Kα radiation (λ=1.5418 Å). Raman spectroscopy was measured on a Renishaw Raman RE01 Microscope with a 633 nm excitation Ar laser. The chemical compositions and the surface electronic states of products were determined by X-ray photoelectron spectroscopy (XPS) using an ESCALAB Xi^+ Thermo Fisher XPS instrument.

Electrochemical Measurements. The electrochemical properties of the products were examined using CR2025 coin-type cells, which were assembled in Ar-filled glove-box with both H_2O and O_2 contents less than 1.0 ppm. The working electrode was prepared by mixing the active materials, acetylene black and polyacrylic acid (PAA, Mw=100000) with a weight ratio of 8/1/1 using deionized water as solvent. The uniformly mixed slurry was coated on a Cu foil and then dried at 70 °C overnight under vaccum, followed by cutting into circular disks with diameter of 14 mm as the working electrodes. The loading of active materials on each coin cell was about 0.67 mg/cm^2. Sodium foil was used as the counter electrode, and Whatman glass fiber membrane was used as separator. The electrolyte was 1M $NaClO_4$ dissolved in a mixed solution of ethylene carbonate/propylene carbonate (EC/PC, 1:1 in volume) with addition of 5 vol.% fluoroethylene carbonates. Cyclic voltammetry (CV) and electrochemical impedance spectroscopy (EIS) were conducted on an Autolab PGSTAT 302N electrochemical workstation, and Galvanostatic charge-discharge tests were carried out on a Neware BTS battery test system.

Author Manuscript

This article is protected by copyright. All rights reserved.

Acknowledgements. This work was supported by the National Science Foundation of China (Grant No. 51402232), the Natural Science Basis Research Plan in Shaanxi Province of China (2018JM5085), the State Key Laboratory of Electrical Insulation and Power Equipment (No. EIPE19127), the Key Laboratory Construction Program of Xi'an Municipal Bureau of Science and Technology (201805056ZD7CG40), the ANU Futures Scheme (Q4601024) and the Australian Research Council (DP190100295, LE190100014), and China Scholarship Council (No. 201906280078) scholarship. We thank Chao Li from the Instrument Analysis Center of Xi'an Jiaotong University for TEM/SEM measurements.

Reference

1. Poizot, P.; Laruelle, S.; Grugeon, S.; Dupont, L.; Tarascon, J. M., *Nature* **2000,** *407* (6803), 496-499. DOI 10.1038/35035045.

2. Tarascon, J. M.; Armand, M., *Nature* **2001,** *414* (6861), 359-367. DOI 10.1038/35104644.

3. Bruce, P. G.; Scrosati, B.; Tarascon, J.-M., *Angewandte Chemie International Edition* **2008,** *47* (16), 2930-2946. DOI 10.1002/anie.200702505.

4. Wang, H.; Wang, J.; Cao, D.; Gu, H.; Li, B.; Lu, X.; Han, X.; Rogach, A. L.; Niu, C., *Journal of Materials Chemistry A* **2017,** *5* (15), 6817-6824. DOI 10.1039/C7TA00772H.

5. Li, W.; Hu, S.; Luo, X.; Li, Z.; Sun, X.; Li, M.; Liu, F.; Yu, Y., *Adv Mater* **2017,** *29* (16). DOI 10.1002/adma.201605820.

6. Tarascon, J. M., *Philosophical transactions. Series A, Mathematical, physical, and engineering sciences* **2010,** *368* (1923), 3227-41. DOI 10.1098/rsta.2010.0112.

7. Lv, C.; Xu, W.; Liu, H.; Zhang, L.; Chen, S.; Yang, X.; Xu, X.; Yang, D., *Small* **2019,** *15* (23), e1900816. DOI 10.1002/smll.201900816.

8. Yabuuchi, N.; Kubota, K.; Dahbi, M.; Komaba, S., *Chemical Reviews* **2014,** *114* (23), 11636-11682. DOI 10.1021/cr500192f.

Author Manuscript

This article is protected by copyright. All rights reserved.

9. Lv, C.; Liu, H.; Li, D.; Chen, S.; Zhang, H.; She, X.; Guo, X.; Yang, D., *Carbon* **2019,** *143*, 106-115. DOI 10.1016/j.carbon.2018.10.091.

10. Wen, Y.; He, K.; Zhu, Y.; Han, F.; Xu, Y.; Matsuda, I.; Ishii, Y.; Cumings, J.; Wang, C., *Nature communications* **2014,** *5*, 4033. DOI 10.1038/ncomms5033.

11. Kim, S.-W.; Seo, D.-H.; Ma, X.; Ceder, G.; Kang, K., *Advanced Energy Materials* **2012,** *2* (7), 710-721. DOI 10.1002/aenm.201200026.

12. Liao, Y.; Wu, C.; Zhong, Y.; Chen, M.; Cai, L.; Wang, H.; Liu, X.; Cao, G.; Li, W., *Nano Research* **2020,** *13* (1), 188-195. DOI 10.1007/s12274-019-2594-2.

13. Zhang, W.; Yue, Z.; Wang, Q.; Zeng, X.; Fu, C.; Li, Q.; Li, X.; Fang, L.; Li, L., *Chemical Engineering Journal* **2020,** *380*, 122548. DOI https://doi.org/10.1016/j.cej.2019.122548.

14. David, L.; Bhandavat, R.; Singh, G., *ACS nano* **2014,** *8* (2), 1759-1770. DOI 10.1021/nn406156b.

15. Wang, H.; Yao, T.; Li, C.; Meng, L.; Cheng, Y., *Chemical Engineering Journal* **2020,** *397*, 125385. DOI https://doi.org/10.1016/j.cej.2020.125385.

16. Zhang, Y.; Wang, N.; Sun, C.; Lu, Z.; Xue, P.; Tang, B.; Bai, Z.; Dou, S., *Chemical Engineering Journal* **2018,** *332*, 370-376. DOI 10.1016/j.cej.2017.09.092.

17. Liang, L.; Xu, Y.; Wang, C.; Wen, L.; Fang, Y.; Mi, Y.; Zhou, M.; Zhao, H.; Lei, Y., *Energy & Environmental Science* **2015,** *8* (10), 2954-2962. DOI 10.1039/C5EE00878F.

18. Li, L.; Peng, S.; Bucher, N.; Chen, H.-Y.; Shen, N.; Nagasubramanian, A.; Eldho, E.; Hartung, S.; Ramakrishna, S.; Srinivasan, M., *Nano Energy* **2017,** *37*, 81-89. DOI 10.1016/j.nanoen.2017.05.012.

19. Yuan, S.; Zhu, Y.-H.; Li, W.; Wang, S.; Xu, D.; Li, L.; Zhang, Y.; Zhang, X.-B., *Advanced Materials* **2017,** *29* (4), 1602469. DOI 10.1002/adma.201602469.

20. Zhang, K.; Park, M.; Zhou, L.; Lee, G.-H.; Shin, J.; Hu, Z.; Chou, S.-L.; Chen, J.; Kang, Y.-M., *Angewandte Chemie International Edition* **2016,** *55* (41), 12822-12826. DOI 10.1002/anie.201607469.

21. Sun, R.; Wei, Q.; Sheng, J.; Shi, C.; An, Q.; Liu, S.; Mai, L., *Nano Energy* **2017,** *35*, 396-404. DOI https://doi.org/10.1016/j.nanoen.2017.03.036.

22. Cho, E.; Song, K.; Park, M. H.; Nam, K.-W.; Kang, Y.-M., *Small* **2016,** *12* (18), 2510-2517. DOI 10.1002/smll.201503168.

Author Manuscript

This article is protected by copyright. All rights reserved.

23. Liu, Z.; Lu, T.; Song, T.; Yu, X.-Y.; Lou, X. W.; Paik, U., *Energy & Environmental Science* **2017,** *10* (7), 1576-1580. DOI 10.1039/C7EE01100H.

24. Liu, J.; Kopold, P.; Wu, C.; van Aken, P. A.; Maier, J.; Yu, Y., *Energy & Environmental Science* **2015,** *8* (12), 3531-3538. DOI 10.1039/c5ee02074c.

25. Choi, S. H.; Kang, Y. C., *ACS applied materials & interfaces* **2015,** *7* (44), 24694-702. DOI 10.1021/acsami.5b07093.

26. Chen, Q.; Sun, S.; Zhai, T.; Yang, M.; Zhao, X.; Xia, H., *Advanced Energy Materials* **2018,** *8* (19), 1800054. DOI 10.1002/aenm.201800054.

27. Wang, Y.; Kang, W.; Cao, D.; Zhang, M.; Kang, Z.; Xiao, Z.; Wang, R.; Sun, D., *Journal of Materials Chemistry A* **2018,** *6* (11), 4776-4782. DOI 10.1039/c8ta00493e.

28. Chen, Z.; Wu, R.; Liu, M.; Wang, H.; Xu, H.; Guo, Y.; Song, Y.; Fang, F.; Yu, X.; Sun, D., *Advanced Functional Materials* **2017,** *27* (38), 1702046. DOI 10.1002/adfm.201702046.

29. Wang, J.; Wang, L.; Eng, C.; Wang, J., *Advanced Energy Materials* **2017,** *7* (14), 1602706. DOI 10.1002/aenm.201602706.

30. Fang, G.; Wu, Z.; Zhou, J.; Zhu, C.; Cao, X.; Lin, T.; Chen, Y.; Wang, C.; Pan, A.; Liang, S., *Advanced Energy Materials* **2018,** *8* (19), 1703155. DOI 10.1002/aenm.201703155.

31. Peng, Q.; Hu, X.; Zeng, T.; Shang, B.; Mao, M.; Jiao, X.; Xi, G., *Chemical Engineering Journal* **2020,** *385*, 123857. DOI 10.1016/j.cej.2019.123857.

32. Zhang, B.; Huang, J.; Kim, J.-K., *Advanced Functional Materials* **2015,** *25* (32), 5222-5228. DOI 10.1002/adfm.201501498.

33. Wei, Z.; Wang, D.; Yang, X.; Wang, C.; Chen, G.; Du, F., *Advanced Materials Interfaces* **2018,** *5* (19), 1800639. DOI 10.1002/admi.201800639.

34. Zhang, W.; Li, J.; Guan, Y.; Jin, Y.; Zhu, W.; Guo, X.; Qiu, X., *Journal of Power Sources* **2013,** *243*, 661-667. DOI 10.1016/j.jpowsour.2013.06.010.

35. Shi, W.; Song, S.; Zhang, H., *Chemical Society reviews* **2013,** *42* (13), 5714-43. DOI 10.1039/c3cs60012b.

36. Yang, L.-X.; Zhu, Y.-J.; Li, L.; Zhang, L.; Tong, H.; Wang, W.-W.; Cheng, G.-F.; Zhu, J.-F., *European Journal of Inorganic Chemistry* **2006,** *2006* (23), 4787-4792. DOI 10.1002/ejic.200600553.

Author Manuscript

This article is protected by copyright. All rights reserved.

37. Dong, G.; Zhao, H.; Xu, Y.; Zhang, X.; Cheng, X.; Gao, S.; Huo, L., *Journal of Alloys and Compounds* **2019,** *785*, 563-572. DOI 10.1016/j.jallcom.2019.01.234.

38. Wang, L.; Cui, X.; Gong, L.; Lyu, Z.; Zhou, Y.; Dong, W.; Liu, J.; Lai, M.; Huo, F.; Huang, W.; Lin, M.; Chen, W., *Nanoscale* **2017,** *9* (11), 3898-3904. DOI 10.1039/C7NR00178A.

39. Cherian, C. T.; Reddy, M. V.; Haur, S. C.; Chowdari, B. V., *ACS applied materials & interfaces* **2013,** *5* (3), 918-23. DOI 10.1021/am302583c.

40. Li, H.; Yang, Q.; Mo, F.; Liang, G.; Liu, Z.; Tang, Z.; Ma, L.; Liu, J.; Shi, Z.; Zhi, C., *Energy Storage Materials* **2019,** *19*, 94-101. DOI 10.1016/j.ensm.2018.10.005.

41. Ren, W.; Zhang, H.; Guan, C.; Cheng, C., *Advanced Functional Materials* **2017,** *27* (32), 1702116. DOI 10.1002/adfm.201702116.

42. Huang, F.; Meng, R.; Sui, Y.; Wei, F.; Qi, J.; Meng, Q.; He, Y., *Journal of Alloys and Compounds* **2018,** *742*, 844-851. DOI 10.1016/j.jallcom.2018.01.324.

43. Baltrusaitis, J.; Mendoza-Sanchez, B.; Fernandez, V.; Veenstra, R.; Dukstiene, N.; Roberts, A.; Fairley, N., *Applied Surface Science* **2015,** *326*, 151-161. DOI https://doi.org/10.1016/j.apsusc.2014.11.077.

44. Miki, Y.; Nakazato, D.; Ikuta, H.; Uchida, T.; Wakihara, M., *Journal of Power Sources* **1995,** *54* (2), 508-510. DOI https://doi.org/10.1016/0378-7753(94)02136-Q.

45. Zhu, K.; Wang, X.; Liu, J.; Li, S.; Wang, H.; Yang, L.; Liu, S.; Xie, T., *ACS Sustainable Chemistry & Engineering* **2017,** *5* (9), 8025-8034. DOI 10.1021/acssuschemeng.7b01595.

46. Jiang, G.; Li, L.; Huang, Z.; Xie, Z.; Cao, B., *Journal of Alloys and Compounds* **2019,** *790*, 891-899. DOI 10.1016/j.jallcom.2019.03.283.

47. Wang, J.; Wang, H.; Li, F.; Xie, S.; Xu, G.; She, Y.; Leung, M. K. H.; Liu, T., *Journal of Materials Chemistry A* **2019,** *7* (7), 3024-3030. DOI 10.1039/c9ta00045c.

48. Xie, S.; Wang, H.; Yao, T.; Wang, J.; Wang, C.; Shi, J. W.; Han, X.; Liu, T.; Cheng, Y., *Journal of colloid and interface science* **2019,** *553*, 320-327. DOI 10.1016/j.jcis.2019.06.039.

49. Wang, J.; Wang, H.; Yao, T.; Liu, T.; Tian, Y.; Li, C.; Li, F.; Meng, L.; Cheng, Y., *Journal of colloid and interface science* **2020,** *560*, 546-554. DOI 10.1016/j.jcis.2019.10.096.

Author Manuscript

This article is protected by copyright. All rights reserved.

50. Xie, J.; Liu, S.; Cao, G.; Zhu, T.; Zhao, X., *Nano Energy* **2013,** *2* (1), 49-56. DOI https://doi.org/10.1016/j.nanoen.2012.07.010.

51. Ouyang, C.; Wang, X.; Wang, S., *Chemical communications* **2015,** *51* (75), 14160-3. DOI 10.1039/c5cc05541e.

52. Faber, M. S.; Dziedzic, R.; Lukowski, M. A.; Kaiser, N. S.; Ding, Q.; Jin, S., *Journal of the American Chemical Society* **2014,** *136* (28), 10053-61. DOI 10.1021/ja504099w.

53. Turner, N. H.; Single, A. M., *Surface and Interface Analysis* **1990,** *15* (3), 215-222. DOI 10.1002/sia.740150305.

54. Kong, W.; Luan, X.; Du, H.; Xia, L.; Qu, F., *Chemical communications* **2019,** *55* (17), 2469-2472. DOI 10.1039/C8CC10203A.

55. Jin, B.; Zhou, X.; Huang, L.; Lickleder, M.; Yang, M.; Schmuki, P., *Angewandte Chemie International Edition* **2016,** *55* (40), 12252-12256. DOI 10.1002/anie.201605551.

56. Shen, L.; Yu, L.; Wu, H. B.; Yu, X. Y.; Zhang, X.; Lou, X. W., *Nature communications* **2015,** *6*, 6694. DOI 10.1038/ncomms7694.

57. Liu, Y.; Kang, H.; Jiao, L.; Chen, C.; Cao, K.; Wang, Y.; Yuan, H., *Nanoscale* **2015,** *7* (4), 1325-1332. DOI 10.1039/C4NR05106H.

58. Bian, H.; Dong, R.; Shao, Q.; Wang, S.; Yuen, M.-F.; Zhang, Z.; Yu, D. Y. W.; Zhang, W.; Lu, J.; Li, Y. Y., *Journal of Materials Chemistry A* **2017,** *5* (45), 23967-23975. DOI 10.1039/c7ta08228b.

59. Choi, S. H.; Kang, Y. C., *Nanoscale* **2016,** *8* (7), 4209-16. DOI 10.1039/c5nr07733h.

60. Xia, X.; Deng, S.; Xie, D.; Wang, Y.; Feng, S.; Wu, J.; Tu, J., *Journal of Materials Chemistry A* **2018,** *6* (32), 15546-15552. DOI 10.1039/c8ta06232c.

61. He, H.; Sun, D.; Tang, Y.; Wang, H.; Shao, M., *Energy Storage Materials* **2019,** *23*, 233-251. DOI 10.1016/j.ensm.2019.05.008.

62. Jiang, Y.; Song, D.; Wu, J.; Wang, Z.; Huang, S.; Xu, Y.; Chen, Z.; Zhao, B.; Zhang, J., *ACS nano* **2019,** *13* (8), 9100-9111. DOI 10.1021/acsnano.9b03330.

63. Zhao, Y.; Pang, Q.; Meng, Y.; Gao, Y.; Wang, C.; Liu, B.; Wei, Y.; Du, F.; Chen, G., *Chemistry – A European Journal* **2017,** *23* (53), 13150-13157. DOI 10.1002/chem.201702399.

Author Manuscript

This article is protected by copyright. All rights reserved.

64. Chang, L.; Wang, K.; Huang, L.-a.; He, Z.; Zhu, S.; Chen, M.; Shao, H.; Wang, J., *J. Mater. Chem. A* **2017,** *5* (39), 20892-20902. DOI 10.1039/c7ta05027e.

65. Peng, S.; Han, X.; Li, L.; Zhu, Z.; Cheng, F.; Srinivansan, M.; Adams, S.; Ramakrishna, S., *Small* **2016,** *12* (10), 1359-68. DOI 10.1002/smll.201502788.

66. Hong, Y. J.; Son, M. Y.; Kang, Y. C., *Advanced Materials* **2013,** *25* (16), 2279-2283. DOI 10.1002/adma.201204506.

67. Qin, Q.; Chen, L.; Wei, T.; Liu, X., *Small* **2019,** *15* (29), e1803639. DOI 10.1002/smll.201803639.

68. Zhu, T.; Wang, J.; Ho, G. W., *Nano Energy* **2015,** *18*, 273-282. DOI https://doi.org/10.1016/j.nanoen.2015.10.035.

69. Wang, J.; Yang, N.; Tang, H.; Dong, Z.; Jin, Q.; Yang, M.; Kisailus, D.; Zhao, H.; Tang, Z.; Wang, D., *Angewandte Chemie International Edition* **2013,** *52* (25), 6417-6420. DOI 10.1002/anie.201301622.

70. Yang, X.; Wang, J.; Wang, S.; Wang, H.; Tomanec, O.; Zhi, C.; Zboril, R.; Yu, D. Y. W.; Rogach, A., *ACS nano* **2018,** *12* (7), 7397-7405. DOI 10.1021/acsnano.8b04114.

71. Zhu, S.; Li, Q.; Wei, Q.; Sun, R.; Liu, X.; An, Q.; Mai, L., *ACS applied materials & interfaces* **2017,** *9* (1), 311-316. DOI 10.1021/acsami.6b10143.

72. Xu, X.; Zhao, R.; Ai, W.; Chen, B.; Du, H.; Wu, L.; Zhang, H.; Huang, W.; Yu, T., *Adv Mater* **2018,** *30* (27), e1800658. DOI 10.1002/adma.201800658.

73. Chao, D.; Liang, P.; Chen, Z.; Bai, L.; Shen, H.; Liu, X.; Xia, X.; Zhao, Y.; Savilov, S. V.; Lin, J.; Shen, Z. X., *ACS nano* **2016,** *10* (11), 10211-10219. DOI 10.1021/acsnano.6b05566.

74. Chao, D.; Zhu, C.; Yang, P.; Xia, X.; Liu, J.; Wang, J.; Fan, X.; Savilov, S. V.; Lin, J.; Fan, H. J.; Shen, Z. X., *Nature communications* **2016,** *7*, 12122. DOI 10.1038/ncomms12122.

75. Brezesinski, T.; Wang, J.; Tolbert, S. H.; Dunn, B., *Nature materials* **2010,** *9* (2), 146-51. DOI 10.1038/nmat2612.

Author Manuscript

This article is protected by copyright. All rights reserved.

Author Manuscript

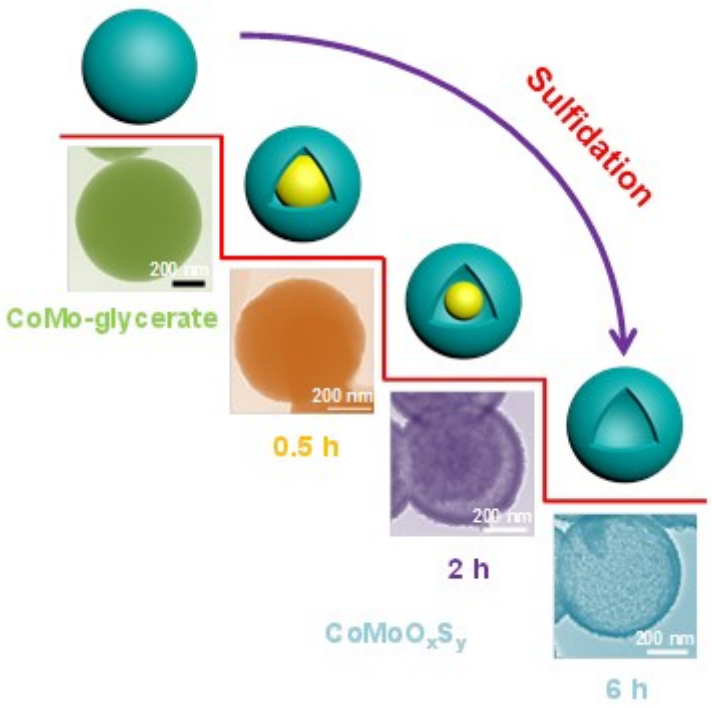

Facile co-engineering on polymorph phases and cavity structures based on CoMo-glycerate by scalable solvothermal sulfidation. The optimized strategy enabled the construction of **an amorphous yolk-shell $CoMoO_xS_y$** with sulfidation-induced amorphous phase and yolk-shell confined cavity. Such $CoMoO_xS_y$ electrode with unique amorphous phase and yolk-shell cavity demonstrate superior cycle capacity and excellent rate capability as an anode material for sodium-ion batteries.

This article is protected by copyright. All rights reserved.